Geophysical Research Letters

RESEARCH LETTER
10.1029/2019GL084649

Significant Impact of Rossby Waves on Air Pollution Detected by Network Analysis

Yongwen Zhang[1,2,3], **Jingfang Fan**[2,4], **Xiaosong Chen**[5], **Yosef Ashkenazy**[1], **and Shlomo Havlin**[2]

[1]Department of Solar Energy and Environmental Physics, The Jacob Blaustein Institutes for Desert Research, Ben-Gurion University of the Negev, Be'er Sheva, Israel, [2]Department of Physics, Bar-Ilan University, Ramat Gan, Israel, [3]Data Science Research Center, Faculty of Science, Kunming University of Science and Technology, Kunming, China, [4]Potsdam Institute for Climate Impact Research, Potsdam, Germany, [5]School of Systems Science, Beijing Normal University, Beijing, China

Key Points:
- Surface pollution variations from China and the United States associated with atmospheric upper air conditions are studied by a network approach
- The upper air critical regimes are found to significantly influence the surface air pollution
- Rossby waves significantly affect air pollution fluctuations through low- and high-pressure systems

Supporting Information:
- Supporting Information S1

Correspondence to:
Y. Zhang,
zhangyongwen77@gmail.com

Citation:
Zhang, Y., Fan, J., Chen, X., Ashkenazy, Y., & Havlin, S. (2019). Significant impact of Rossby waves on air pollution detected by network analysis. *Geophysical Research Letters*, *46*, 12,476–12,485. https://doi.org/10.1029/2019GL084649

Received 22 JUL 2019
Accepted 31 AUG 2019
Accepted article online 6 SEP 2019
Published online 3 NOV 2019

Abstract Air pollution fluctuations have been found to strongly depend on the weather dynamics. Here we identify the significant atmospheric processes that affect the local daily variability of air pollution. We develop a multilayered network analysis to detect the interlinks between the 500-hPa geopotential height and surface air pollution in both China and the United States. We find that Rossby waves significantly affect air pollution fluctuations through the development of cyclone and anticyclone systems and further affect the local stability of the air and the winds. Some of these systems are remote (~3,000 km) and lead to air pollution 1–2 days later. Thus, the impact of Rossby waves on human life is greater than previously believed. The rapid warming of the Arctic could slow down Rossby waves, thus increasing human health risks. Our method can help to determine the risk assessment of such extreme events and can improve potential predictability.

Plain Language Summary Outdoor air pollution plays an important role in a wide range of environmental and health problems. The impact of weather dynamics (at different pressure levels) on the daily fluctuations of air pollution is still not clear. Here we develop a novel multilayer and multivariable network method to delineate the influence of the upper air dynamics on the temporal variability of surface air pollution. We show that the underlying mechanism of our observed relation between weather and air pollution is the dynamics of planetary Rossby waves that not only cause extreme weather events but also lead to strong fluctuations in air pollution. The developed method is applied on data from China and the United States and can help to improve the prediction of extreme pollution events.

1. Introduction

During the last two decades, complex network approaches have been applied to a wide range of disciplines for studying complex systems (Barabási & Albert, 1999; Cohen & Havlin, 2010; Newman, 2018). Network approaches have been found useful for detecting and better understanding the statistical and dynamical features of complex systems (Helbing et al., 2006). In climate networks, geographical locations or observation sites can be regarded as nodes, and their interactions can be quantified as links. The strength of the links is determined by the level of similarity between climate variables (such as temperature, pressure, and precipitation) determined, for example, by cross correlations. Climate network techniques have been successfully applied to improve our understanding of climate phenomena such as the El Niño/Southern Oscillation, the North Atlantic Oscillation, and Rossby waves (Donges et al., 2009; Fan et al., 2017; Guez et al., 2012; Tsonis & Swanson, 2008; Wang et al., 2013; Yamasaki et al., 2008). Climate networks have also been used to forecast extreme climate events (Boers et al., 2014; Ludescher et al., 2014). Furthermore, network approaches can provide a new way to detect and evaluate the impacts of past and future climate change (Fan et al., 2018). A global rainfall teleconnection pattern related to upper-level Rossby waves has been recently revealed using complex network analysis (Boers et al., 2019).

Outdoor air pollution plays an important role in widespread environmental and health problems. Life expectancy is closely related to air quality (Heft-Neal et al., 2018). Fine particulate matter, $PM_{2.5}$, of an aerodynamic diameter of 2.5 μm or less, is a very harmful air pollutant to human health and has been associated with lung cancer and heart diseases (Burnett et al., 2014). It is responsible for most of the global mortality

caused by outdoor air pollution (Cohen et al., 2017). This is especially significant in developing countries due to their rapid economic development and the corresponding rapid increase in anthropogenic aerosol emission. The major sources of particulate matter pollution are both anthropogenic and natural, including traffic emissions, industrial production, biomass burning, agricultural activities, and dust (Zhang & Cao, 2015). In recent years, China has experienced increasingly frequent and persistent haze events caused by high $PM_{2.5}$ concentrations (Zhang & Cao, 2015). Millions of premature deaths have been associated with outdoor air pollution in China. Even in a developed country like the United States, there are still thousands of premature deaths every year due to outdoor air pollution (Lelieveld et al., 2015). Air pollution of aerosol can also potentially affect the weather and the climate system (Guo et al., 2017; Zhang et al., 2013; Li et al., 2017; Qian et al., 2009).

Atmospheric circulations can cause particulate matter to be transported thousands of kilometers (Liu et al., 2009). Goods and services produced in one region for consumption in another (interregional trade) can also substantially contribute to the local particulate matter concentration (Zhang et al., 2017). Quantifying the contributions from the various sources has become a central issue in air pollution studies (Zhang et al., 2016). However, the variability of particulate matter pollution does not only depend on the sources. Previous studies suggested that air pollution variability strongly depends on meteorological conditions (Cai et al., 2017; Tai et al., 2010). Extreme air pollution events were associated with weak surface winds, a shallow boundary layer, temperature inversion, and more (Li et al., 2017; Lou et al., 2019). Such weather conditions could be linked to a common atmospheric mechanism in the upper air. For example, it was suggested that most hazy days in the North China Plain are associated with a local anticyclone in the midtroposphere (Chen et al., 2019). Thus, it is important to identify and quantify the connections between air pollution and the atmospheric dynamics of the middle and upper air levels.

Here, we perform a multilayer and multivariable network analysis in attempt to identify the interlinks between the 500-hPa geopotential height and surface air pollution; this is aimed at quantifying the influence of the upper air dynamics on the temporal variability of surface air pollution. We mainly consider the $PM_{2.5}$ concentrations in three regions: China and the western and eastern United States. The detrended daily observation grids of $PM_{2.5}$ and the geopotential heights are used to construct networks (sections 2 and 3). We identify two multilayered networks, one with dominant anticorrelated interlinks (between geopotential heights and pollution) and one with positively correlated interlinks, corresponding to negative and positive weights, respectively (section 3). Upper air critical regions are quantified by measuring the out-degree of each upper air node associated with the total weights of the significant outgoing interlinks to the ground nodes of pollution. Furthermore, affected regions on the ground are quantified by the in-degree of each ground node associated with the total weights of the significant incoming interlinks from the upper air nodes.

2. Data

The daily average surface mass concentrations of $PM_{2.5}$ in 364 cities across China from 2015 to 2017 are measured by the Chinese Ministry of Environmental Protection (http://113.108.142.147:20035/emcpublish/). Most of the cities are in eastern China. The daily mean surface $PM_{2.5}$ concentrations measured in ~1,000 sites in the United States from 2013 to 2017 were provided by the Environmental Protection Agency Air Quality System (https://www.epa.gov/outdoor-air-quality-data/). Since the zonal extent of the United States is large enough, we considered two regions: the western and eastern United States. The air pollution sites are evenly distributed, and we interpolated the data onto $2.5° \times 2.5°$ grids. The grid points that included more than 5% missing values were omitted, resulting in N_A=95, 31, and 63 grid points for China, and the eastern and western United States, respectively. The geopotential height data are from the global ERA-Interim reanalysis ($2.5° \times 2.5°$) of the European Center for Medium-Range Weather Forecasts (Dee et al., 2011). To filter out trivial seasonal effects, we first detrended the original data by subtracting the corresponding centered 30-day "moving" means and then normalized by the standard deviation of these 30 days (see Leung et al., 2018; Tai et al., 2010).

3. Method

The detrended daily surface $PM_{2.5}$ concentration of grid point i and the geopotential height (500 hPa) of grid point j are represented by time series $A_i(t)$ and $M_j(t)$ during a time period T. The fluctuation series are

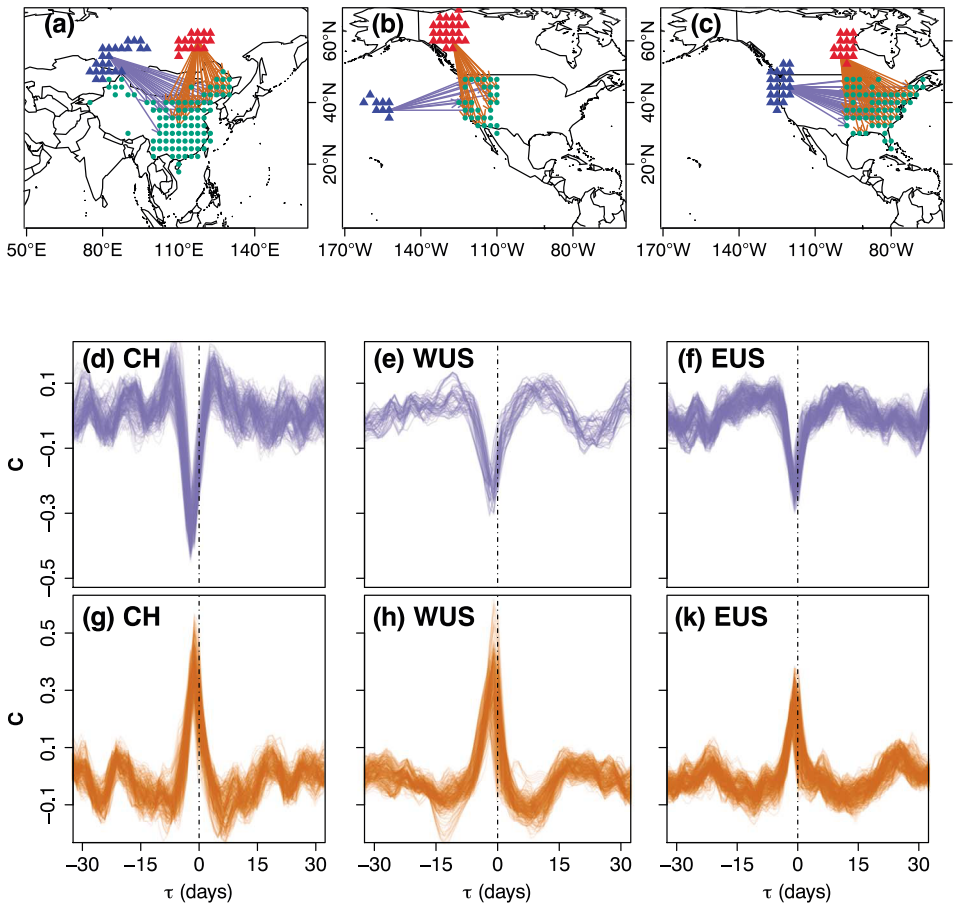

Figure 1. (a–c) The multilayered maps. Blue triangles represent the strongest 10% negative (negatively correlated) out-degree nodes (outgoing from the upper-level nodes), and red triangles are the strongest 10% positive out-degree nodes in the upper air. The interlinks (blue and red arrows) are between the 500-hPa geopotential height and the surface $PM_{2.5}$ concentration (green points). To avoid overlapping, all red triangles are moved 15° to the north. The lower six panels depict the cross-correlation functions of the negative and positive networks' interlinks (blue and red curves) for (d, g) China, (e, h) the western United States, and (f, k) the eastern United States, respectively.

$\delta A_i(t) = A_i(t) - \langle A_i \rangle$ and $\delta M_j(t) = M_j(t) - \langle M_j \rangle$, where $\langle A_i \rangle$ and $\langle M_i \rangle$ are temporal averages for the period T. The cross-correlation function between the two variables for grids i and j is defined as

$$C_{A_i,M_j}(\tau) = \frac{\langle \delta A_i(t-\tau) \cdot \delta M_j(t) \rangle}{\sqrt{\langle [\delta A_i(t-\tau)]^2 \rangle} \cdot \sqrt{\langle [\delta M_j(t)]^2 \rangle}}, \quad (1)$$

where the time lag τ is constrained to be within $-\tau_{max} \le \tau \le \tau_{max}$ where $\tau_{max} = 90$ days. We identify the maximal absolute value of $C_{A_i,M_j}(\tau)$ and denote the corresponding time lag as τ^* (Figures 1d–1k). The direction of the link $C_{A_i,M_j}(\tau^*)$ is from A_i to M_j when $\tau^* > 0$ and from M_j to A_i when $\tau^* < 0$. The direction is undefined when $\tau^* = 0$.

Based on Fan et al. (2017) and Yamasaki et al. (2008), we quantify the strength of the correlations using

$$W_{A_i,M_j} = \frac{C_{A_i,M_j}(\tau^*) - \text{mean}(C_{A_i,M_j}(\tau))}{\text{std}(C_{A_i,M_j}(\tau))}, \quad (2)$$

where "mean" and "std" represent the mean and standard deviation of the cross-correlation function, respectively.

We choose a threshold of W to be Δ=4.5, for which the link strength is considered to be significant; this is based on shuffled data significance tests. The weight W as a function of τ^* and distance r also supports the reliability of the threshold (supporting information Figure S1). Because the negative and positive weights have different properties, we introduce two nonsquare matrices $\boldsymbol{X}^p$ and $\boldsymbol{X}^n$ to describe the interlinks of the positively and negatively correlated multilayer networks, respectively. The element $X^p_{i,j}$ will equal 1, if $W_{A_i,M_j} \geqslant \Delta$ and $\tau^* < 0$ otherwise $X^p_{i,j}$ is 0. In the same way, the element $X^n_{i,j}$ will equal 1, if $W_{A_i,M_j} \leqslant -\Delta$ and $\tau^* < 0$; otherwise $X^n_{i,j}$ is 0.

In this study, the nodes of the network are defined to be the grid cells of either the surface air pollution or of the upper air geopotential height. Then, the negative and positive out-degrees of node (grid) j for the geopotential height are calculated by

$$O^n_{M_j} = \sum_{i=1}^{N_A} X^n_{i,j} W_{A_i,M_j} \ ,$$
$$O^p_{M_j} = \sum_{i=1}^{N_A} X^p_{i,j} W_{A_i,M_j} \ . \tag{3}$$

For the air pollution, we have negative and positive in-degrees of node (grid) i:

$$I^n_{A_i} = \sum_{j=1}^{N_M} X^n_{i,j} W_{A_i,M_j} \ ,$$
$$I^p_{A_i} = \sum_{j=1}^{N_M} X^p_{i,j} W_{A_i,M_j} \ . \tag{4}$$

Obviously, the outgoing links of the geopotential height are the same as the incoming links of the air pollution in a multilayer network. In order to describe the significance of the nodes in the two layers, the out- and in-degrees measure the number of strong outgoing and incoming links from and to the geopotential height nodes and the air pollution nodes, respectively.

4. Results

Figures 1a–1c present the strongest 10% out-degree nodes of the positively correlated and negatively correlated multilayered networks composed of the 500-hPa geopotential height and the surface air $PM_{2.5}$ concentration. The interlinks direction is toward the air pollution nodes at the surface. The weights of the interlinks are obtained from the cross-correlation functions (shown in Figures 1d–1k). The blue triangles at 500 hPa reveal strong anticorrelations with the air pollution nodes. Significant negative peaks are observed for all three regions (Figures 1d–1f). Most of the negative peaks are found for time lags of −1 or −2 days, indicating that changes of the 500-hPa geopotential height occur 1 or 2 days before the correspondingly opposite changes in the surface $PM_{2.5}$ concentration. In contrast, the interlinks of the positive multilayered network between the 500-hPa geopotential height and the surface air $PM_{2.5}$ concentration indicate that the correlation functions have strong positive peaks with a −1 day time delay (Figures 1g–1k), meaning that a high geopotential height is observed ~1 day before a high level of surface $PM_{2.5}$ concentration. In the western and eastern United States, the above interlinks are connected to most of the ground nodes. In China, the interlinks are mainly connected to parts of North China region including the region of Beijing-Tianjin-Hebei that has been severely and frequently exposed to $PM_{2.5}$ pollution in recent years (Zhang & Cao, 2015). Our results indicate that these regions are strongly influenced by the synoptic of the upper air. We note that we did not find significant nodes over the entire North China Plain, especially in the southern part of North China Plain. We obtain similar results for the PM_{10} concentration (supporting information Figure S2).

Figures 2a–2c show the probability distribution function (PDF) of the time lag of the interlinks for China and the western and eastern United States, respectively. For China (Figure 2a), the maximum probability of the time lag is at −2 days for the negative correlations. All other distributions show the maximum values at −1 days. The PDFs in Figures 2a–2c show a decay to 0 after approximately 4 days, indicating that the maximal influence time of the geopotential height on the $PM_{2.5}$ level is 4 days in China and about 3 days in the United States. This difference could be associated to the faster jet stream in the United States. We also calculate the PDF of the geographical lengths of the interlinks (shown in Figures 2d–2f). Two peaks are found around 1,000 km (more than 10°) and 3,000 km (more than 30°) for the positive and negative interlinks,

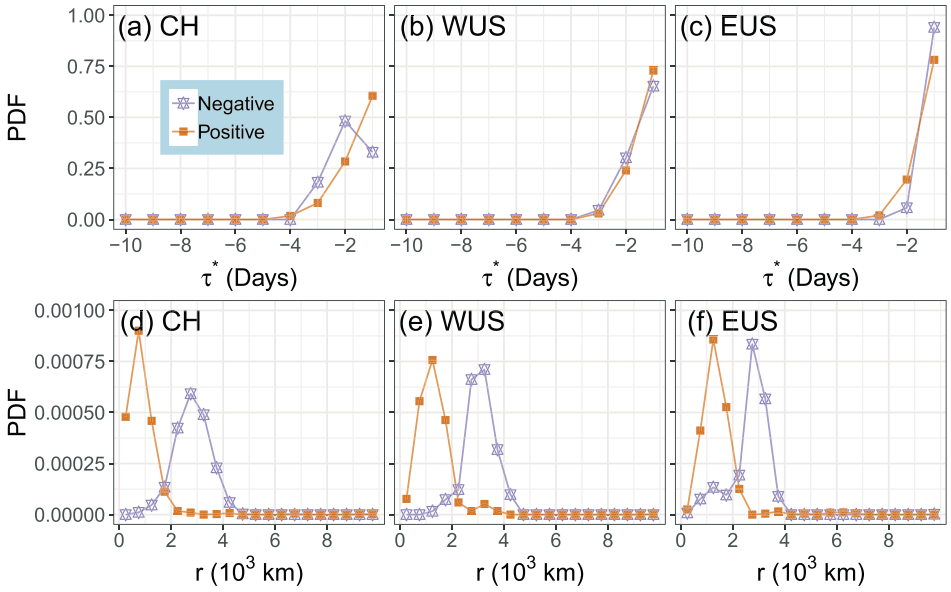

Figure 2. Interlinks statistics: (a–c) PDF of the time lag $\tau^* < 0$ of the interlinks, and (d–f) PDF of the geographical length of the interlinks for China and the western and eastern United States, respectively. PDF = probability distribution function.

respectively. Based on (Chang, 2002; Wang et al., 2013), we suggest that the distributions of the distances are related to atmospheric Rossby waves whose wavelengths vary from around 5,000 to 7,000 km. The longer distances of the negative interlinks (~3,000 km) seem to correspond to half a wavelength of the Rossby wave. The peak in the short distances of the positive interlinks (~1,000 km) could be associated with a typical cyclonic scale within the Rossby wave pattern.

To further support the association of the observed network pattern with Rossby waves, we compare the location of out-degree nodes with the contours of the geopotential height at 500 hPa whose meandering shapes can generally describe the amplitude and phase of a Rossby wave (i.e., corresponding to a ridge or trough Wirth et al., 2018). We consider the mean geopotential height of two extreme cases of days that are 1 day before extremely low (the lowest 10% of days in each month) and extremely high (the top 10% of days in each month) $PM_{2.5}$ concentration days over northeastern China and the western and eastern United States. Figures 3a–3c show the contours of the mean geopotential height for the extremely low air pollution cases,

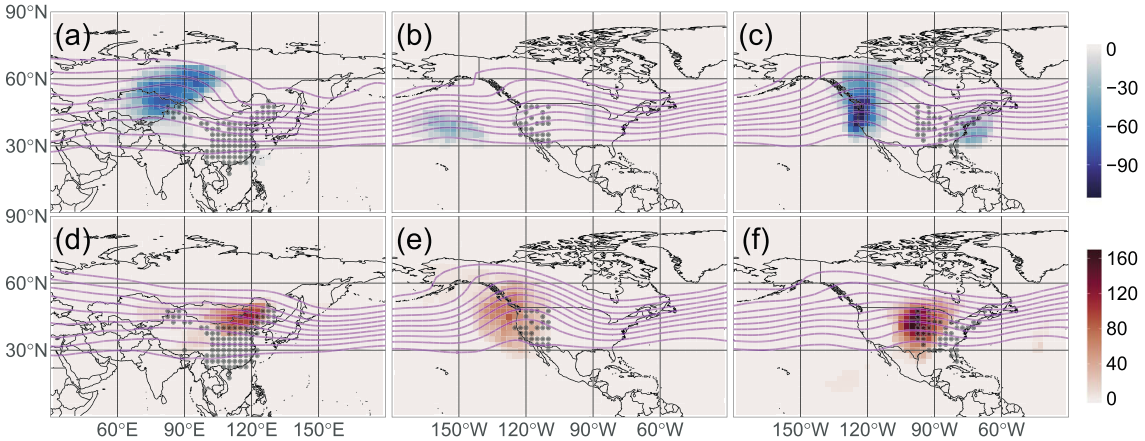

Figure 3. Maps of the 500-hPa geopotential height: Distributions of (a–c) negative and (d–f) positive out-degrees in the upper air for China and the western and eastern United States. Pink contours depict the mean geopotential height of two extreme cases of days with (a–c) extremely low and (d–f) extremely high $PM_{2.5}$ concentrations. The values of the contours increase from north to south within a range of 5,300 to 5,700 m. Gray circles show the locations of the surface $PM_{2.5}$ nodes.

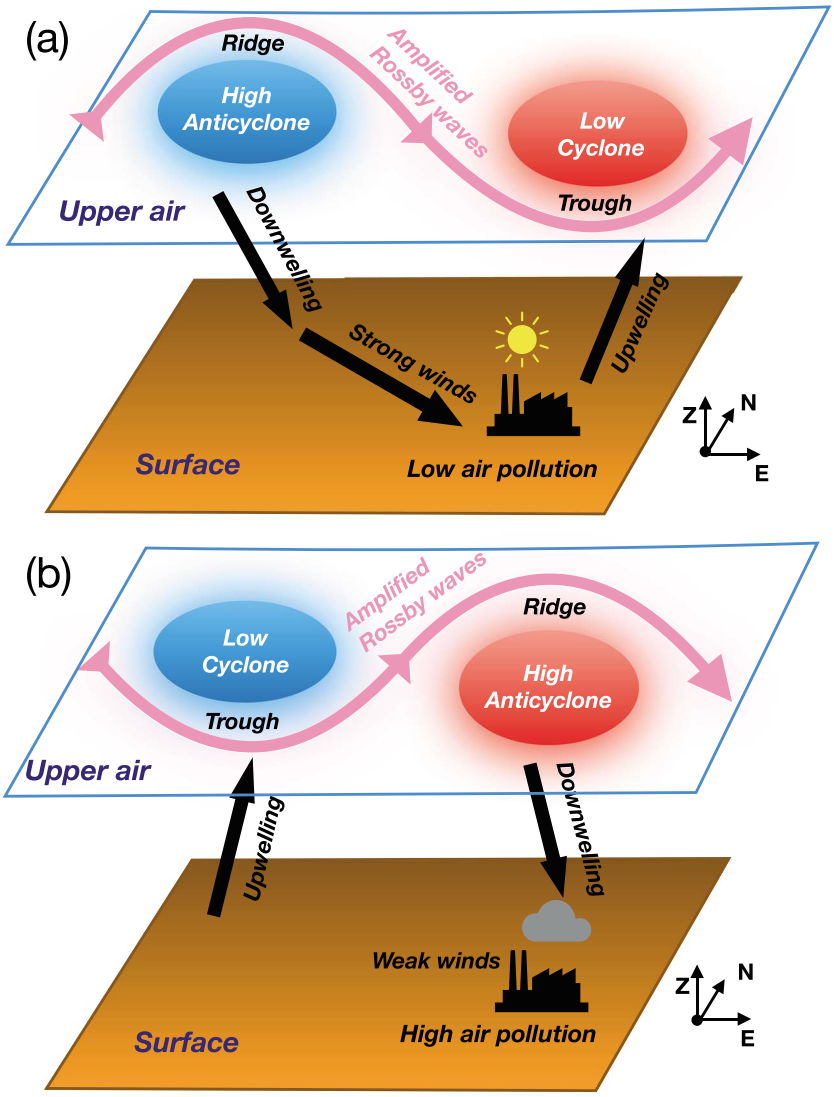

Figure 4. Schematic representation of the atmospheric mechanism caused by Rossby waves. Panels (a) and (b) correspond to low and high air pollution conditions, respectively. See the text for further details.

and Figures 3d–3f show the extremely high air pollution cases in the above three regimes. The localized nodes of the strongest negative out-degree links (over China) are found to be in Russia (Figure 3a). Interestingly, in the same region, the contours of geopotential height form a ridge for the low air pollution days. A trough is also found for the low air pollution days in the east, associated with the red positive nodes of out-degrees, shown in Figure 3d. During the high air pollution days, the contours show a small ridge in the vicinity of the red positive cluster (Figure 3d), and the ridge in Russia disappears. Previous studies also found that the anticyclonic circulations have significant effects on the air quality in China (Chen et al., 2019; Miao et al., 2017; Zhu et al., 2018) and that the Siberian high leads to reduced air pollution in North China (Li et al., 2019; Yin & Wang, 2017); our results are consistent with these studies. The U.S. networks exhibit similar results. Yet, the air pollution over the western and eastern United States is affected by different (upper air) ridges and troughs (Figures 3b, 3c, 3e, and 3f), leading to the different daily variations of air pollution in the western and the eastern United States (Tai et al., 2010). The out-degrees of the networks are generally in accordance with the ridges and troughs (associated with Rossby waves), suggesting that these are important regions in the upper air that influence the surface air pollution. Note that we obtained similar patterns when using the geopotential heights of 300, 700, and 850 hPa (supporting information Figures S4, S6, and S8); yet, the color bar in Figure S8 spans a larger range, indicating a stronger correlation; in general,

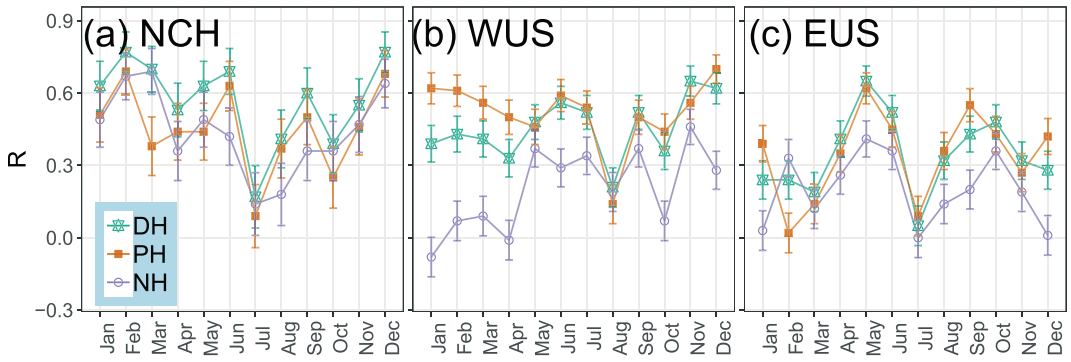

Figure 5. (color online) Pearson correlation coefficient R between the geopotential heights *DH*, *PH*, *NH*, and the daily averaged $PM_{2.5}$ concentration with a 1-day delay over (a) northeastern China, (b) the western United States, and (c) the eastern United States , for different months in the year. The R value of NH is multiplied by −1. The standard error bar is given by $\sqrt{\frac{1-R^2}{n-2}}$.

we observe stronger correlations for higher geopotential height levels (i.e., closer to the surface); the blue and red clusters in Figure S8 slightly move to the east relative to the results of Figure 3. The in-degree patterns are also shown (in supporting information Figures S3, S5, S7, and S9).

Next, we propose a mechanism for the impact of Rossby waves on surface air pollution. Two extreme phases are considered here and depicted schematically in Figure 4. The blue and red colors represent the negative and positive out-degree clusters, respectively. The negative ones are usually located to the west of the air pollution nodes. This can be understood by the high geopotential height that precedes the low-pollution events and since the winds blow from west to east in jet streams. The flow often meanders to the north and south to form ridges and troughs caused by Rossby waves. For the phase of the Rossby wave depicted in Figure 4a, an anticyclone emerges on the (left) ridge, leading to downwelling, while, at the same time, a cyclone develops on the (right) trough near the pollution areas, leading to upwelling. In addition, a high-pressure system develops at the surface, to the west of the air pollution nodes (supporting information Figure S10). The downwelling air to the west of the pollution nodes and the upwelling air in the vicinity of the pollution nodes intensify the westerly winds, which effectively disperse the air pollutants. Moreover, the cyclone (and its upwelling air) near the pollution nodes carries pollutants to the upper air, decreasing surface pollutants. For the opposite phase of the Rossby wave depicted in Figure 4b, the anticyclone and the cyclone switch their locations. Downwelling changes to upwelling in the west, which diverts part of the surface westerly wind upward, hence weakening the surface winds (supporting information Figure S10). In the vicinity of the pollution location, the (eastern) anticyclone causes the upper air to downwell. As a result, the adiabatic warming of the descending air coupled with radiative cooling at the surface produces a temperature inversion layer, and the boundary layer is low, leading to a stable air column that traps the pollutants close to the surface, hence leading to severe pollution. In particular, apparently, severe air pollution events could occur even when the jet stream is less meander (see Figure 3d), indicating that other factors can affect the level of pollution. We believe that due to the high emission of air pollutants in China, even weaker weather systems may lead to severe air pollution. Thus, the upper air out-degree field of the multilayered network provides important information regarding the daily variability of surface air pollution. Potentially, the time delay of the links and their strength may also be useful as a predictive tool.

We next test the monthly effects on the interactions between the geopotential heights and the air pollution. We denote the daily averaged negative and positive geopotential heights (discussed above) as NH and PH, respectively, in the upper air nodes (the blue and red triangles shown in Figure 1). We also denote the difference between the geopotential height as DH=PH−NH in order to test the potential predictive power when considering both the negative and positive patterns. The specific scatter plots and the corresponding correlation curves of the daily averaged $PM_{2.5}$ concentration (with a 1-day delay) versus DH are shown in supporting information Figures S11–S13. Most of the months display good linear relations. Figure 5 shows their Pearson correlation coefficient R. The R values of DH are almost always the highest, especially over northeastern China where the R value is usually larger than 0.5. For several months, the R values of DH over the western United States are similar to PH; this can be attributed to the weak anticorrelation and

predominant positive correlation patterns. We note that the *R* values during the summer (July and August) are significantly lower than in other months for all regions. This is probably since the jet stream and the winds are much weaker during the summer months (Archer & Caldeira, 2008; Woollings et al., 2010), resulting in weaker interactions between the upper air and ground pollution. In general, when considering both the negative and positive patterns, taking the difference between them (DH) can provide a better predictive tool. Similar results for the different geopotential height levels are found in supporting information Figures S14–S16.

5. Conclusions

Indeed, most sources of air pollutants are anthropogenic. Yet, the variability of air pollution strongly depends on atmospheric processes. Here, we have found that the response of the $PM_{2.5}$ pollution to the geopotential height of 500 hPa is significant. We identify the corresponding upper air regions using network analysis and quantify their influence; there are two localized areas (western and eastern) in both China and the United States. The western region is anticorrelated with the surface air pollution nodes, while, in contrast, the eastern region (which is closer to the pollution region) is positively correlated with the upper air pollution nodes. We suggest that the underlying mechanism is related to Rossby waves that are associated with meanders of the midlatitude jet stream and with ridges and troughs of the upper air geopotential height, leading to high-pressure (anticyclonic) and low-pressure (cyclonic) systems. Thus, the amplitudes and phases of Rossby waves substantially affect air pollution on the ground. Furthermore, the difference of geopotential height between the two regions has a potential predictive power.

Earlier studies (Petoukhov et al., 2013; Screen & Simmonds, 2014) demonstrated the statistical connection between high-amplitude Rossby waves and extreme weather events on the ground. These include heat and cold waves that occurred in the Northern Hemisphere midlatitudes during the past decade. Here, we show that pronounced Rossby waves not only cause extreme weather events but also lead to stronger fluctuations of air pollution. The two extreme phases of Rossby waves lead to low and high surface pollution. Since the Arctic sea ice extent is rapidly declining, the warming in this region is occurring faster than in the rest of the Northern Hemisphere, leading to a decreasing meridional temperature gradient that could cause the jet stream and winds to weaken (Archer & Caldeira, 2008). Therefore, a slower eastward propagation of Rossby waves may develop (Francis & Vavrus, 2012), which could be associated with more prolonged extreme weather events and may lead in the future, as suggested by the present study, to more prolonged air pollution events (Cai et al., 2017). Actually, the impact of the changes of atmospheric circulations on haze pollution in China has been discussed earlier (Yin & Wang, 2017), and a significant interdecadal variability of pollution has been associated with the generation of the meridional wind over East China related to interannual variation of winter haze pollution (Chen et al., 2019).

The interlinks of the multilayered network can be used to quantify the relationship between the upper troposphere and the surface pollution. We find here indications that the amplitudes and phases of Rossby waves influence the surface air pollution. Our study not only provides significant spatial patterns at different levels but also shows time shifts between the levels that can help to determine the risk assessment of extreme events in space and improve potential predictability. Our method can also be used to study other interactions of weather patterns between the atmosphere and the surface.

Acknowledgments
We thank Dean Chen for helpful discussions. We thank the Italian Ministry of Foreign Affairs and International Cooperation, and the Israeli Ministry of Science, Technology, and Space; the Israel Science Foundation, ONR, Japan Science Foundation, BSF-NSF, ARO, the EU H2020 project RISE, and DTRA (Grant HDTRA-1-10-1-0014) for financial support. We also acknowledge the data resources provided by the Ministry of Environmental Protection of China (http://113.108.142.147:20035/emcpublish/) and U.S. Environmental Protection Agency (https://www.epa.gov/outdoor-air-quality-data/). J. F. acknowledges the "East Africa Peru India Climate Capacities—EPICC" project, which is part of the International Climate Initiative (IKI). The Federal Ministry for the Environment, Nature Conservation and Nuclear Safety (BMU) supports this initiative on the basis of a decision adopted by the German Bundestag. The Potsdam Institute for Climate Impact Research (PIK) is leading the execution of the project together with its project partners The Energy and Resources Institute (TERI) and the Deutscher Wetterdienst (DWD).

References

Archer, C. L., & Caldeira, K. (2008). Historical trends in the jet streams. *Geophysical Research Letters*, *35*, L08803. https://doi.org/10.1029/2008GL033614

Barabási, A. L., & Albert, R. (1999). Emergence of scaling in random networks. *Science*, *286*(5439), 509–512. https://doi.org/10.1126/SCIENCE.286.5439.509

Boers, N., Bookhagen, B., Barbosa, H. M., Marwan, N., Kurths, J., & Marengo, J. A. (2014). Prediction of extreme floods in the eastern Central Andes based on a complex networks approach. *Nature Communications*, *5*(1), 5199. https://doi.org/10.1038/ncomms6199

Boers, N., Goswami, B., Rheinwalt, A., Bookhagen, B., Hoskins, B., & Kurths, J. (2019). Complex networks reveal global pattern of extreme-rainfall teleconnections. *Nature*, *566*(7744), 373–377. https://doi.org/10.1038/s41586-018-0872-x

Burnett, R. T., Arden Pope, C., Ezzati, M., Olives, C., Lim, S. S., Mehta, S., et al. (2014). An integrated risk function for estimating the global burden of disease attributable to ambient fine particulate matter exposure. *Environmental Health Perspectives*, *122*(4), 397–403. https://doi.org/10.1289/ehp.1307049

Cai, W., Li, K., Liao, H., Wang, H., & Wu, L. (2017). Weather conditions conducive to Beijing severe haze more frequent under climate change. *Nature Climate Change*, *7*(4), 257–262. https://doi.org/10.1038/nclimate3249

Chang, E. K. M. (2002). Characteristics of wave packets in the upper troposphere. Part I: Seasonal and hemispheric variations. *Journal of the Atmospheric Sciences*, *56*(11), 1729–1747.

Chen, S., Guo, J., Song, L., Cohen, J. B., & Wang, Y. (2019). Temporal disparity of the atmospheric systems contributing to interannual variation of wintertime haze pollution in the North China Plain. *International Journal of Climatology*, 1–17. https://doi.org/10.1002/joc.6198

Chen, S., Guo, J., Song, L., Li, J., Liu, L., & Cohen, J. B. (2019). Inter-annual variation of the spring haze pollution over the North China Plain: Roles of atmospheric circulation and sea surface temperature. *International Journal of Climatology*, *39*(2), 783–798. https://doi.org/10.1002/joc.5842

Cohen, A. J., Brauer, M., Burnett, R., Anderson, H. R., Frostad, J., Estep, K., et al. (2017). Estimates and 25-year trends of the global burden of disease attributable to ambient air pollution: An analysis of data from the Global Burden of Diseases Study 2015. *Lancet*, *389*(10082), 1907–1918. https://doi.org/10.1016/S0140-6736(17)30505-6

Cohen, R., & Havlin, S. (2010). Complex networks: Structure, robustness, and function. https://doi.org/10.1007/s13398-014-0173-7.2

Dee, D. P., Uppala, S. M., Simmons, A. J., Berrisford, P., Poli, P., Kobayashi, S., et al. (2011). The ERA-Interim reanalysis: Configuration and performance of the data assimilation system. *Quarterly Journal of the Royal Meteorological Society*, *137*(656), 553–597. https://doi.org/10.1002/qj.828

Donges, J. F., Zou, Y., Marwan, N., & Kurths, J. (2009). The backbone of the climate network. *EPL*, *87*(4), 48007. https://doi.org/10.1209/0295-5075/87/48007

Fan, J., Meng, J., Ashkenazy, Y., Havlin, S., & Schellnhuber, H. J. (2017). Network analysis reveals strongly localized impacts of El Niño. *Proceedings of the National Academy of Sciences of the United States of America*, *114*(29), 7543–7548. https://doi.org/10.1073/pnas.1701214114

Fan, J., Meng, J., Ashkenazy, Y., Havlin, S., & Schellnhuber, H. J. (2018). Climate network percolation reveals the expansion and weakening of the tropical component under global warming. *Proceedings of the National Academy of Sciences of the United States of America*, *115*(52), E12128–E12134. https://doi.org/10.1073/pnas.1811068115

Francis, J. A., & Vavrus, S. J. (2012). Evidence linking Arctic amplification to extreme weather in mid-latitudes. *Geophysical Research Letters*, *39*, L06801. https://doi.org/10.1029/2012GL051000

Guez, O., Gozolchiani, A., Berezin, Y., Brenner, S., & Havlin, S. (2012). Climate network structure evolves with North Atlantic Oscillation phases. *EPL*, *98*(3), 38006. https://doi.org/10.1209/0295-5075/98/38006

Guo, J., Su, T., Li, Z., Miao, Y., Li, J., Liu, H., et al. (2017). Declining frequency of summertime local-scale precipitation over eastern China from 1970 to 2010 and its potential link to aerosols. *Geophysical Research Letters*, *44*, 5700–5708. https://doi.org/10.1002/2017GL073533

Heft-Neal, S., Burney, J., Bendavid, E., & Burke, M. (2018). Robust relationship between air quality and infant mortality in Africa. *Nature*, *559*(7713), 254–258. https://doi.org/10.1038/s41586-018-0263-3

Helbing, D., Armbruster, D., Mikhailov, A. S., & Lefeber, E. (2006). Information and material flows in complex networks. *Physica*, *363*(1), 1–160. https://doi.org/10.1016/j.physa.2006.01.042

Lelieveld, J., Evans, J. S., Fnais, M., Giannadaki, D., & Pozzer, A. (2015). The contribution of outdoor air pollution sources to premature mortality on a global scale. *Nature*, *525*(7569), 367–371. https://doi.org/10.1038/nature15371

Leung, D. M., Tai, A. P., Mickley, L. J., Moch, J. M., Van Donkelaar, A., Shen, L., & Martin, R. V. (2018). Synoptic meteorological modes of variability for fine particulate matter ($PM_{2.5}$) air quality in major metropolitan regions of China. *Atmospheric Chemistry and Physics*, *18*(9), 6733–6748. https://doi.org/10.5194/acp-18-6733-2018

Li, Z., Guo, J., Ding, A., Liao, H., Liu, J., Sun, Y., et al. (2017). Aerosol and boundary-layer interactions and impact on air quality. *National Science Review*, *4*(6), 810–833. https://doi.org/10.1093/nsr/nwx117

Li, J., Liao, H., Hu, J., & Li, N. (2019). Severe particulate pollution days in China during 2013-2018 and the associated typical weather patterns in Beijing-Tianjin-Hebei and the Yangtze River Delta regions. *Environmental Pollution*, *248*, 74–81. https://doi.org/10.1016/j.envpol.2019.01.124

Liu, J., Mauzerall, D. L., & Horowitz, L. W. (2009). Evaluating inter-continental transport of fine aerosols:(2) Global health impact. *Atmospheric Environment*, *43*(28), 4339–4347. https://doi.org/10.1016/j.atmosenv.2009.05.032

Lou, M., Guo, J., Wang, L., Xu, H., Chen, D., Miao, Y., et al. (2019). On the relationship between aerosol and boundary layer height in summer in China Under different thermodynamic conditions. *Earth, Planets and Space*, *6*(5), 2019EA000620. https://doi.org/10.1029/2019EA000620

Ludescher, J., Gozolchiani, A., Bogachev, M. I., Bunde, A., Havlin, S., & Schellnhuber, H. J. (2014). Very early warning of next El Niño. *Proceedings of the National Academy of Sciences of the United States of America*, *111*(6), 201323058. https://doi.org/10.1073/pnas.1323058111

Miao, Y., Guo, J., Liu, S., Liu, H., Li, Z., Zhang, W., & Zhai, P. (2017). Classification of summertime synoptic patterns in Beijing and their associations with boundary layer structure affecting aerosol pollution. *Atmospheric Chemistry and Physics*, *17*(4), 3097–3110. https://doi.org/10.5194/acp-17-3097-2017

Newman, M. (2018). *Networks*. New York: Oxford University Press.

Petoukhov, V., Rahmstorf, S., Petri, S., & Schellnhuber, H. J. (2013). Quasiresonant amplification of planetary waves and recent Northern Hemisphere weather extremes. *Proceedings of the National Academy of Sciences of the United States of America*, *110*(14), 5336–5341. https://doi.org/10.1073/pnas.1222000110

Qian, Y., Gong, D., Fan, J., Leung, L. R., Bennartz, R., Chen, D., & Wang, W. (2009). Heavy pollution suppresses light rain in China: Observations and modeling. *Journal of Geophysical Research*, *114*, D00K02. https://doi.org/10.1029/2008JD011575

Screen, J. A., & Simmonds, I. (2014). Amplified mid-latitude planetary waves favour particular regional weather extremes. *Nature Climate Change*, *4*(8), 704–709. https://doi.org/10.1038/nclimate2271

Tai, A. P., Mickley, L. J., & Jacob, D. J. (2010). Correlations between fine particulate matter ($PM_{2.5}$) and meteorological variables in the United States: Implications for the sensitivity of $PM_{2.5}$ to climate change. *Atmospheric Environment*, *44*(32), 3976–3984. https://doi.org/10.1016/j.atmosenv.2010.06.060

Tsonis, A. A., & Swanson, K. L. (2008). Topology and predictability of El Niño and la Niña Networks. *Physical Review Letters*, *100*(22), 228502. https://doi.org/10.1103/PhysRevLett.100.228502

Wang, Y., Gozolchiani, A., Ashkenazy, Y., Berezin, Y., Guez, O., & Havlin, S. (2013). Dominant imprint of Rossby waves in the climate network. *Physical Review Letters*, *111*(13), 138501. https://doi.org/10.1103/PhysRevLett.111.138501

Wirth, V., Riemer, M., Chang, E. K. M., & Martius, O. (2018). Rossby wave packets on the midlatitude waveguide—A review. *Monthly Weather Review*, *146*(7), 1965–2001. https://doi.org/10.1175/MWR-D-16-0483.1

Woollings, T., Hannachi, A., & Hoskins, B. (2010). Variability of the North Atlantic eddy-driven jet stream. *Quarterly Journal of the Royal Meteorological Society*, *136*(649), 856–868. https://doi.org/10.1002/qj.625

Yamasaki, K., Gozolchiani, A., & Havlin, S. (2008). Climate networks around the globe are significantly affected by El Niño. *Physical Review Letters*, *100*(22), 228501. https://doi.org/10.1103/PhysRevLett.100.228501

Yin, Z., & Wang, H. (2017). Role of atmospheric circulations in haze pollution in December 2016. *Atmospheric Chemistry and Physics*, *17*(18), 11,673–11,681. https://doi.org/10.5194/acp-17-11673-2017

Zhang, Y. L., & Cao, F. (2015). Fine particulate matter ($PM_{2.5}$) in China at a city level. *Scientific Reports*, *5*(1), 14884. https://doi.org/10.1038/srep14884

Zhang, R., Delworth, T. L., Sutton, R., Hodson, D. L. R., Dixon, K. W., Held, I. M., et al. (2013). Have aerosols caused the observed atlantic multidecadal variability? *Journal of the Atmospheric Sciences*, *70*(4), 1135–1144. https://doi.org/10.1175/JAS-D-12-0331.1

Zhang, Q., Jiang, X., Tong, D., Davis, S. J., Zhao, H., Geng, G., et al. (2017). Transboundary health impacts of transported global air pollution and international trade. *Nature*, *543*(7647), 705–709. https://doi.org/10.1038/nature21712

Zhang, L., Shao, J., Lu, X., Zhao, Y., Hu, Y., Henze, D. K., et al. (2016). Sources and processes affecting fine particulate matter pollution over North China: An adjoint analysis of the Beijing APEC period. *Environmental Science & Technology*, *50*(16), 8731–8740. https://doi.org/10.1021/acs.est.6b03010

Zhu, W., Xu, X., Zheng, J., Yan, P., Wang, Y., & Cai, W. (2018). The characteristics of abnormal wintertime pollution events in the Jing-Jin-Ji region and its relationships with meteorological factors. *Science of the Total Environment*, *626*, 887–898. https://doi.org/10.1016/j.scitotenv.2018.01.083